



HAL
open science

Teleseismic traveltimes residuals across the Dead Sea basin

R. Hofstetter, Catherine Dorbath

► **To cite this version:**

R. Hofstetter, Catherine Dorbath. Teleseismic traveltimes residuals across the Dead Sea basin. *Journal of Geophysical Research : Solid Earth*, 2014, pp.doi:10.1002/2014JB011357. 10.1002/2014JB011357 . hal-01172525

HAL Id: hal-01172525

<https://hal.science/hal-01172525>

Submitted on 8 Jul 2021

HAL is a multi-disciplinary open access archive for the deposit and dissemination of scientific research documents, whether they are published or not. The documents may come from teaching and research institutions in France or abroad, or from public or private research centers.

L'archive ouverte pluridisciplinaire **HAL**, est destinée au dépôt et à la diffusion de documents scientifiques de niveau recherche, publiés ou non, émanant des établissements d'enseignement et de recherche français ou étrangers, des laboratoires publics ou privés.

Copyright

RESEARCH ARTICLE

10.1002/2014JB011357

Key Point:

- Teleseismic traveltime residuals in the Dead Sea basin

Correspondence to:

A. Hofstetter,
ramih@gii.co.il

Citation:

Hofstetter, A., and C. Dorbath (2014), Teleseismic traveltimes residuals across the Dead Sea basin, *J. Geophys. Res. Solid Earth*, 119, 8884–8899, doi:10.1002/2014JB011357.

Received 6 JUN 2014

Accepted 31 OCT 2014

Accepted article online 5 NOV 2014

Published online 4 DEC 2014

Teleseismic traveltimes residuals across the Dead Sea basin

A. Hofstetter^{1,2} and C. Dorbath^{2,3}

¹Geophysical Institute of Israel, Lod, Israel, ²Ecole et Observatoire des Sciences de la Terre, Strasbourg, France, ³IRD, Toulouse, France

Abstract New findings of the structure of the Dead Sea sedimentary basin and its eastern and western bordering regions are obtained by *P* and *PKP* wave relative traveltime residuals of 644 teleseisms, as recorded by the Dead Sea Integrated Research portable seismic network in the Dead Sea basin and its neighboring regions. The Lisan Peninsula is characterized by relatively small teleseismic traveltime residuals of about 0.14 s, in the latitude range of 31.22°–31.37° and at the longitude of 35.50°, slowly decreasing toward the west. The largest teleseismic traveltime residuals are in the southern Dead Sea basin, south of the Lisan Peninsula in the latitude range of 31.05°–31.15° and along longitude 35.45° and continuing southward toward the Amaziahu Fault, reaching values of 0.4–0.5 s. There is a small positive residual at the Amaziahu Fault and a small negative residual south of it probably marking the southern end of the Dead Sea basin. East and west of the Dead Sea basin the mean teleseismic traveltime residuals are negative with overall averages of –0.35 s and –0.45 s, respectively. Using the teleseismic residuals, we estimate the horizontal dimensions of the Lisan salt diapir to be 23 km × 13 km at its widest and a maximal thickness of about 7.2 km. The thickness of the Mount Sodom salt diapir is estimated as 6.2 km.

1. Introduction

Observations of teleseismic events can be a useful tool for obtaining a better understanding of the structure of the area under study or the velocity contrast across a fault. In particular, the use of teleseismic traveltime residuals is advantageous. The success of this method is due to the almost vertical arrivals of the incident waves, which provide an integration of the medium below the seismic stations. The method was also applied in other regions, e.g., the Kilauea Volcano in Hawaii, [Ellsworth and Koyanagi, 1977], the Coso geothermal area in California [Reasenberget al., 1980], the Central Africa Shear zone in Cameroon, the San Andreas, and Calaveras faults in California [Dorbath et al., 1986, 1996], across the Dead Sea fault in California [Hofstetter et al., 2000], and across the 1944 rupture zone of the North Anatolian fault in Turkey [Ozakin et al., 2012]. All these studies used a relatively small number of stations, obtaining only general information on the structures or the physical dimensions of large features.

The Dead Sea Integrated Research (DESIRE) campaign in the Dead Sea basin (DSB) and its bordering regions aimed to study the seismotectonics of the basin (Figure 1). For achieving this goal, the DESIRE campaign included a large number of stations in a relatively small area, unlike the studies mentioned above. In this study we use many teleseismic observations of the dense network of the DESIRE campaign in the Dead Sea basin, supported with the results of three wide-angle reflection/refraction profiles that were recently conducted in the DSB (Figure 1), to obtain a better definition of the physical dimensions of major features in the basin. Below, we specifically focus our attention on the Lisan and Mount Sodom salt diapirs, and the location of the Bokek and Ein Gedi transverse faults.

2. Tectonic Setting of the Dead Sea Basin

In this section we briefly describe the tectonic setting of the Dead Sea basin and its bordering regions. In addition, we focus below on three wide-angle refraction/reflection profiles that were conducted in the Dead Sea basin, to be used as a support for our interpretation. The Dead Sea basin (DSB) is the largest basin within the Dead Sea fault (DSF), where the Dead Sea lake covers only part of the whole basin. The DSB is often modeled as a pull-apart basin, where the nearly north-south oriented Jericho and Arava faults, two large segments of the DSF, bound it on the west and east, respectively [e.g., Neev and Hall 1979; Garfunkel, 1981; Garfunkel et al., 1981;

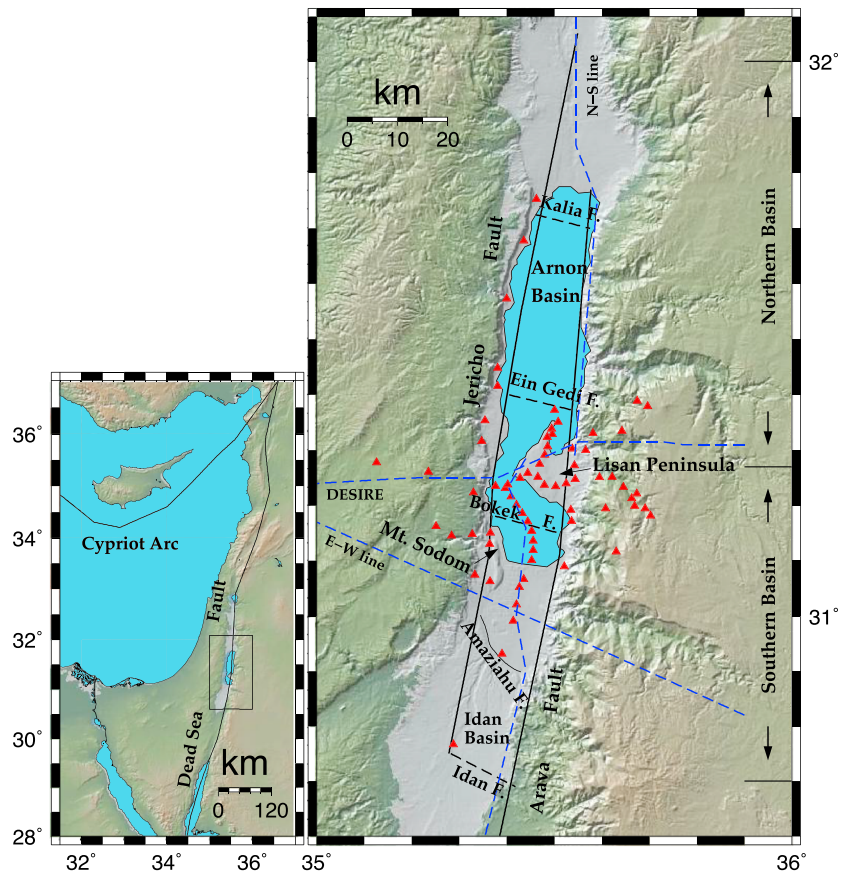


Figure 1. (left) Schematic map of the Eastern Mediterranean Sea including the Dead Sea fault; rectangle indicates area enlarged on the right; (right) tectonic setting of the DSB along with the main tectonic features, subbasins, and schematic faults (F. refers to fault; black solid lines or black dashed lines where inferred) in the Dead Sea basin [after Neev and Hall, 1979; Ben-Avraham and ten Brink, 1989; Lazar, 2004; Bartov et al., 2004; Lazar et al., 2006; Ben-Avraham et al., 2008, 2010; Hofstetter et al., 2008]. Red triangles present the DESIRE temporary stations. The northern and southern subbasins are separated by the Lisan Peninsula (latitude 31.25°N) which is also indicated, where the Dead Sea lake covers only part of the whole basin. Blue dash lines present the E-W, N-S, and DESIRE wide-angle reflection/refraction (WRR) profiles of Ten Brink et al. [2006]; Ten Brink and Flores [2012], and Mechie et al. [2009], respectively.

Sagy et al., 2003; Petrunin and Sobolev, 2006, 2008], which overlap in the DSB to form two en echelon strike-slip faults (Figure 1). The actual extension of these segments is not well known. The basin is closed at its southern end by a series of normal faults, the most visible being the Amaziyah fault, oriented NW-SE, which exhibits at least 50 m of downdip displacement, with a pronounced subsurface continuation [Kashai and Croker, 1987; Ben-Avraham, 1997; Al-Zoubi et al., 2002; Ginzburg et al., 2006]. Frieslander [2000] and Ben-Avraham et al. [2008] suggested that Idan fault, about 20 km south of Amaziyah fault, is probably the southern end of the basin. No normal fault has been evidenced at the northern end of the basin [Garfunkel, 1981], while within the basin transverse faulting is observed [Lazar, 2004; Ben-Avraham et al., 2008, 2010]. The Lisan Peninsula, a large buried salt diapir, separates the DSB into two main subbasins, a northern and a southern one, where topography of the Lisan Peninsula is slightly raised above the basin. Tectonics has shaped the Dead Sea fault in general and the Dead Sea basin in particular over the past few million years [e.g., Freund et al., 1970; Ben-Menahem et al., 1976; Garfunkel, 1981]. Many seismological, geophysical (i.e., refraction, reflection, and gravity) and geological studies have provided important information about the structure and the velocity structure of the DSB and adjacent regions [e.g., Garfunkel et al., 1981; Van Eck and Hofstetter, 1989, 1990; Rotstein et al., 1991; Aldersons et al., 2003; Frieslander, 2000; Shamir et al., 2005; Koulakov and Sobolev, 2006; Shamir, 2006; Al-Zoubi et al., 2007; Hofstetter et al., 2007; Mohsen et al., 2011; Braeuer et al., 2012a, 2012b, 2014; Kaviani et al., 2013].

Ten Brink et al. [2006] and Ten Brink and Flores [2012] reported the results of two wide-angle reflection/refraction (WRR) profiles (called also the E-W and N-S lines) which were conducted in 2004. The E-W line crossed the basin

Table 1. DESIRE Stations That Are Used in This Study; J or I, and S or B (in Station Name Column) Are for Jordan or Israel, and Short Period or Broadband, Respectively

No.	Station Name	Latitude (°N)	Longitude (°E)	Altitude (m)	No.	Station Name	Latitude (°N)	Longitude (°E)	Altitude (m)
1	JB01	31.23710	35.47915	-330	34	JB39	31.19470	35.60761	670
2	JB02	31.25192	35.46523	-331	35	JS40	31.11655	35.63011	1096
3	JS03	31.25877	35.44380	-331	36	JB41	31.27262	35.54250	-233
4	JB04	31.24997	35.42810	-385	37	IS01	31.27769	35.126145	533
5	JS05	31.23783	35.40220	-389	38	IS02	31.260524	35.234549	614
6	JS06	31.27531	35.46942	-318	39	IS08	31.235332	35.376277	-391
7	JB07	31.29146	35.47960	-330	40	IB09	31.231218	35.396592	-390
8	JS08	31.30699	35.48604	-352	41	IS10	31.215945	35.408608	-386
9	JS09	31.32339	35.48528	-345	42	IB11	31.201048	35.420185	-395
10	JB10	31.33855	35.49455	-394	43	IS12	31.186023	35.432131	-390
11	JS11	31.35122	35.50832	-395	44	IB13	31.171217	35.444040	-395
12	JB12	31.37247	35.50018	-393	45	IS14	31.153986	35.452216	-395
13	JS13	31.23487	35.50288	-330	46	IB15	31.136359	35.455273	-390
14	JS14	31.23980	35.52475	-288	47	IS16	31.11923	35.455472	-390
15	JB15	31.24745	35.54355	-215	48	IB17	31.101002	35.452280	-388
16	JS17	31.25093	35.59520	234	49	IB19	31.066879	35.435838	-385
17	JB18	31.25148	35.62162	411	50	IS20	31.052111	35.426091	-382
18	JB19	31.23319	35.64560	540	51	IB21	31.02075	35.420533	-380
19	JS20	31.21314	35.66253	574	52	IS27	31.145183	35.283961	90
20	JB21	31.19888	35.66875	753	53	IB22	31.062582	35.364652	-270
21	JS22	31.19445	35.69124	787	54	IB25	31.130217	35.363633	-320
22	JS23	31.22128	35.67334	665	55	IB31	31.316577	35.347416	-100
23	JS24	31.18134	35.70216	958	56	IS32	31.35350	35.354031	-270
24	JB25	31.08933	35.52062	-336	57	IS34	31.074711	35.332702	0
25	JS26	31.17172	35.53622	-358	58	IS35	30.990871	35.413377	-374
26	JS27	31.19172	35.53495	-344	59	IB36	30.931260	35.389620	-331
27	JS28	31.30299	35.53738	-338	60	IS37	31.416150	35.380630	-390
28	JB29	31.30007	35.56571	-160	61	IB38	31.448970	35.380940	-300
29	JS31	31.33068	35.58116	119	62	IS40	31.150690	35.365100	-363
30	JS33	31.33458	35.64223	991	63	IS41	30.767070	35.287930	-150
31	JS35	31.37906	35.69644	902	64	IS42	31.573220	35.399540	-250
32	JS36	31.42189	35.73890	811	65	IS43	31.67816	35.435390	-313
33	JB37	31.38895	35.67463	875	66	IB44	31.752690	35.462600	-320

at latitude 31°N, just north of Amaziah fault (E-W line in Figure 1). The N-S line was aligned with the Dead Sea fault from about 50 km north of the Dead Sea Lake to about 120 km south of the lake. They defined the low-density layer in the southern DSB as the upper crust, suggesting that the fault continues down to 18 km. They also reported that there is no indication of a low-velocity anomaly extending into the lower crust under the DSB. The DESIRE project examined the DSB and its bordering regions, in general, and the southern DSB in particular, comprising 66 seismic stations in the passive part of the project (Figure 1). The very dense network of DESIRE, especially in the southern Dead Sea basin, enabled detailed seismological studies, i.e., spatial distribution of seismicity and local earthquake tomography [Braeuer et al., 2012a, 2012b, 2014]. In the active part of DESIRE, Mechie et al. [2009] conducted an E-W seismic profiling, crossing the Lisan Peninsula along latitude 31.3°N, which marks the border between the southern and northern Dead Sea subbasins (DESIRE profile in Figure 1). They reported that the upper and lower crust boundary is at 20 km. The northern subbasin is characterized by a sedimentary sequence (basin and prebasin sediments) of about 6 km, which thickens under the Lisan Peninsula to about 12 km, shallows to about 8 km near the Amaziah fault and to about 2 km of prebasin sediments near the Idan fault [Ben-Avraham and Ginzburg, 1990; Hofstetter et al., 1991, 2000; Gardosh et al., 1997; Ten Brink et al., 2006; Mechie et al., 2009; Ten Brink and Flores, 2012].

The above-mentioned refraction cross sections of the Dead Sea basin studies showed gradual changes of the Moho depth under the southern DSB and its bordering regions. South of the lake, Ten Brink et al. [2006] reported Moho values of 33 km, 31 km, and 29 km at about 30 km east of the DSB, under the DSB, and about 20 km west of the basin, respectively. Along latitude 31.3°N, crossing the Lisan Peninsula, Mechie et al. [2009] reported Moho values of 32 km, 32 km, and 33 km at about 30 km east of the DSB, under the Lisan

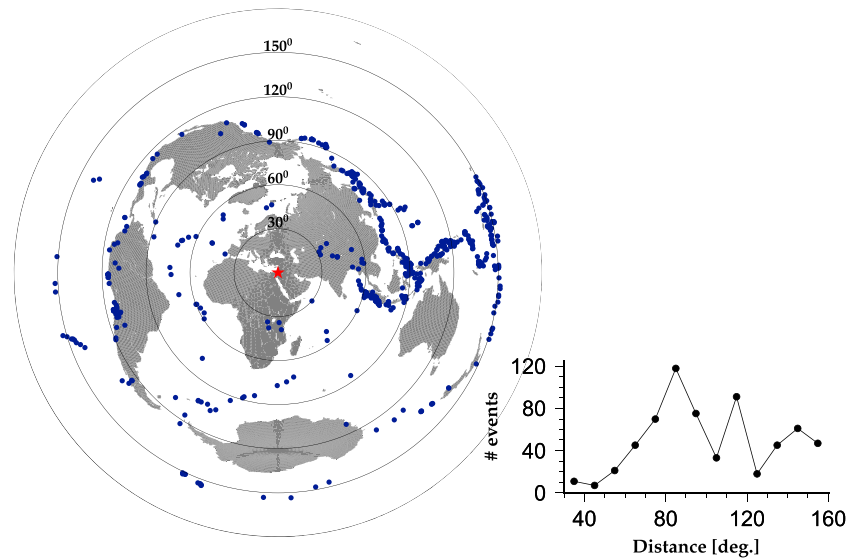


Figure 2. (left) Distribution of teleseismic events (blue circles) with magnitude greater than 5.0 that were recorded by the DESIRE network (red star). The equidistant circles show distances in degrees to the center of the DESIRE network. See text for more details; (right) number of events as a function of distance, within an interval of $\pm 5^\circ$, from the center of the DESIRE network.

Peninsula, and about 20 km west of the Lisan Peninsula, respectively. Those studies are in accordance with earlier refraction studies on both sides of the basin [Ginzburg *et al.*, 1979a, 1979b, 1979c; El-Isa *et al.*, 1987; El-Isa, 1990] or results of local earthquake tomography [Koulakov and Sobolev, 2006]. Ten Brink *et al.* [2006], Ten Brink and Flores [2012], and Mechie *et al.* [2009] reported that at depths from 20 km to the Moho at about 32 km under the DSB there are no changes of the lower crust and any perturbation of Moho topography is within the data resolution.

The Dead Sea Rift Transect (DESERT) project, being active from May 2001 to February 2002, was composed of a 260 km long transect extending from the Mediterranean coast to the Arabian platform [Weber and DESERT Group, 2004; Weber, 2005; Weber and DESIRE group, 2009]. The central part of the transect crosses the DSF at a location in the Arava Valley which is about 60 km south of the Dead Sea lake [Mechie *et al.*, 2005]. Using the observed data of DESERT, Koulakov *et al.* [2006] reported that there is no reliable signature of the Dead Sea Transform in the upper mantle structure. Based on all the refraction profiles, Mechie *et al.* [2009] suggested that the Dead Sea pull-apart basin is essentially an upper crustal feature with upper crustal extension, and below about 20 km the two plates move past each other in a shearing motion. Consequently, any major observed travelt ime anomaly is due to variations in seismic velocities of the upper crust inside the basin and on both sides.

3. Method of Analysis and Teleseismic Data Reduction

The DESIRE project aimed to study the DSB and its bordering regions, in general, and the southern Dead Sea basin in particular, comprising 66 stations from October 2006 to April 2008, having about an equal number of broadband (BB) and short period (SP) seismometers (Figure 1 and Table 1). The main advantage in using the DESIRE stations is the high density of stations in the southern Dead Sea basin (SDSB) and the Lisan Peninsula with typical separation of 2 km between neighboring stations, and on the eastern and western flanks of the basin typical separation of less than 7 km between neighboring stations, having a total number of 60 stations in this area, and another six stations in the bordering regions. In comparison, there are only five permanent stations of the Israel Seismic Network (ISN) and the Jordan Seismic Observatory (JSO) in the Lisan Peninsula and the SDSB, and only another five stations in all the other parts of the Dead Sea basin combined, with a typical separation of over 20 km between neighboring stations. In addition, near each permanent station of ISN and JSO in the SDSB and the Lisan Peninsula a DESIRE station was installed, not more than 100 m away. The majority of the stations were installed either on the Dead Sea dams, which surround the evaporation ponds in the

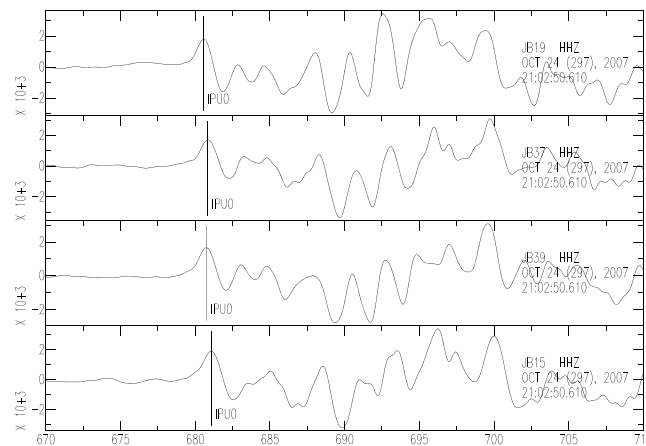


Figure 3. Example of recordings at four DESIRE stations of M_w 6.8 earthquake on 24 October 2007, latitude 3.90°S , longitude 101.02°E (near Sumatra), distance of 71.5° from the center of the network. Time is relative to the origin of the earthquake.

there is still a significant number of earthquakes in the quadrants west of the network to be used in the analysis. The source parameters of these events are determined by the National Earthquake Information Center, U.S. Geological Survey (<http://earthquake.usgs.gov/regional/neic>).

A total of about 37,000 P wave arrivals are read from the recordings of the short-period and broadband vertical component seismic stations. For each event, all traces were visually compared and correlated using distinct phases such as P (about 60% of all phases), or PP (about 20%), or PKP (about 20%), and if possible, we also checked prominent phases such as pP or $pPKP$ immediately following the distinct phase. If the earthquake occurred at a distance of 98° or less, we use the P phase (see Figure 2) [Storchak *et al.*, 2003]. For larger distances we use the clearest phase between PP and PKP . The sampling rate of the SP and BB stations are 200 sps and 100 sps, respectively. Thus, the picking error is estimated to be less than 0.02 s. We discarded doubtful readings, i.e., seismograms with unclear phases, corrupted seismograms, and noisy seismograms. Because of the relatively small size of the network, systematic errors, caused by event mislocation, and variation of the ray path shapes to the seismic stations, are estimated to be less than 0.01 s [Engdahl *et al.*, 1977]. Figure 3 shows four (out of 66) recordings of DESIRE stations of a strong earthquake that occurred near Sumatra on 24 October 2007. We observe high similarity of the recordings at all stations. In the next phase we use waveform cross correlation to measure accurate arrival times of all the stations relative to a reference one. To ensure high-quality signals, not contaminated by external noise, we discarded stations for which the correlation values were less than 0.8.

Considering that the geological structures on either side of the DSB are not identical, we corrected all travel time residuals due to the different altitudes of the stations by moving them to the level of the Dead Sea lake (-400 m below sea level). Using results of crustal refraction and wide-angle reflection/refraction (WRR) studies [Ginzburg *et al.*, 1979a, 1979b; Ginzburg and Folkman, 1980; Ten Brink *et al.*, 2006; Mechie *et al.*, 2009; Ten Brink and Flores, 2012], velocities of 3.8 km/s and 3.5 km/s are assigned for the western and eastern sides, respectively.

The paths to the stations either near the earthquake source or in the deeper parts of the mantle, away from the stations, are essentially identical. Moreover, examining the E-W and N-S lines, and the DESIRE WRR profile, it is clear that the upper mantle and lower crust are rather similar [Ten Brink *et al.*, 2006; Mechie *et al.*, 2009; Mohsen *et al.*, 2011; Ten Brink and Flores, 2012]. Changes in the arrival times among the stations are the superposition of two factors: (1) being located at different distances relative to the epicenter and (2) variations in the structure of the upper crust underneath the stations. To eliminate the first factor, we calculated the theoretical travel time from the source to each station and also to the center of the network, thus applying a moveout correction.

To account for the second factor, we examine two upper crust columns that represent the structure inside the Dead Sea basin, and two columns that represent the shoulders of the basin (Figure 4). The columns that

southern Dead Sea basin, or in the Lisan Peninsula, and thus providing an excellent opportunity to conduct measurements in the middle of the basin.

The data set of the DESIRE project comprises 644 earthquakes, which occurred throughout the Dead Sea basin at the distance range of 30° – 154° in the magnitude range of 5.0–8.5 (Figure 2), where the majority ($\sim 80\%$) of the teleseisms range from 75° to 150° , thus ensuring almost vertical arrivals of the incident waves. There is an abundant number of strong earthquakes from the northeast and southeast quadrants (mainly western and central Pacific Ocean and eastern Asia), versus less strong earthquakes from other quadrants, i.e., the Atlantic Ocean (Figure 2). However,

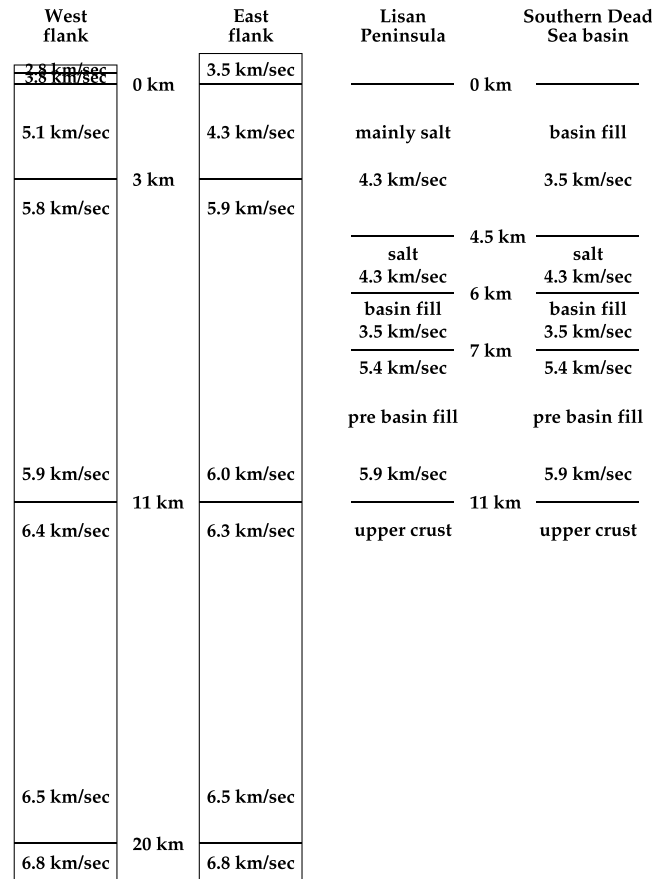


Figure 4. (left) Typical upper crustal columns of the eastern and western flanks of the Dead Sea basin [after *Mechie et al., 2009*]; (right) typical upper part of the upper crust columns of the Lisan Peninsula (salt diapir) and Southern Dead Sea basin [after *Ten Brink and Flores, 2012*, and references therein]. Numbers inside the columns present *P* velocity and numbers in between columns present the depth of a given boundary. See text for further details.

represent the shoulders of the basin are based on the DESIRE WRR profile [Mechie et al., 2009]. Below a depth of 3 km, they are rather similar, and the variations of *P* velocity in the upper part of the upper crust are due to different rock composition [Segev et al., 2006, and references therein]. The Lisan Peninsula column (actually Lisan salt diapir column) and the Southern Dead Sea basin (SDSB) column represent columns inside the basin, are based on the N-S line that traverses the Dead Sea basin [Ten Brink and Flores, 2012, Figure 6, and references therein]. The SDSB column and the Lisan Peninsula column present the sedimentary sequence in the upper part of the upper crust just north of the E-W WRR profile [Ten Brink et al., 2006], and the sedimentary sequence in the Lisan Peninsula based on the N-S WRR profile [Ten Brink and Flores, 2012] near the crossing with the DESIRE WRR profile, respectively. The total thickness of each column is about 11 km. The columns are similar except the upper layer in the SDSB column that is composed of basin fill with typical *P* velocity of 3.5 km/s or mainly salt in the Lisan salt diapir column with *P* velocity of 4.3 km/s [Al-Zoubi and ten Brink, 2001]. Due to the relatively slow material in the SDSB column it is considered to be a “slow” column while the Lisan column with *P*

velocity 4.3 km/s is a “fast” column leading to longer traveltimes and shorter traveltimes, respectively. The *P* velocities in the layers in the columns that represent the shoulders on both sides of the basin are larger than the *P* velocities in the columns inside the Dead Sea basin at any given depth in the upper crust (Figure 4) [see also Ten Brink et al., 2006, Figure 1; Mechie et al., 2009, Figure 11; Ten Brink and Flores, 2012, Figure 6], and the difference in the *P* velocities can be up to 1 km/s. Thus, relative to the columns in the basin the columns that represent shoulders of the Dead Sea basin are significantly faster.

In order to minimize the source effect resulting from incorrect hypocenter location and origin time and to minimize effects due to any lack of homogeneity along the raypaths away from the study area, we use travel time residuals. The raw teleseismic traveltime residuals are given by $t_{ij} = T_{ij}(\text{obs}) - T_{ij}(\text{theor})$ for the *i*th station and *j*th event, and the theoretical time is calculated using IASP91 model [Kennett and Engdahl, 1991]. The relative traveltime residual is $r_{ij} = t_{ij} - \bar{t}_j$ for a given event, where the mean residual \bar{t}_j is the average of observed arrivals for event *j*. The mean relative teleseismic traveltime residual for each station \bar{r}_i is the average of all traveltime residuals of all events [i.e., Ellsworth and Koyanagi, 1977; Reasenberget al., 1980]. Each of the analyzed events was recorded by at least six stations, and usually by more than 20 stations. The mean teleseismic traveltime residuals are obtained by averaging several dozen residual values (>50) and usually several hundred, implying a small scatter of errors due to varying the number of observations for a given event, and ruling out the dependence of the average residual on any subset of stations.

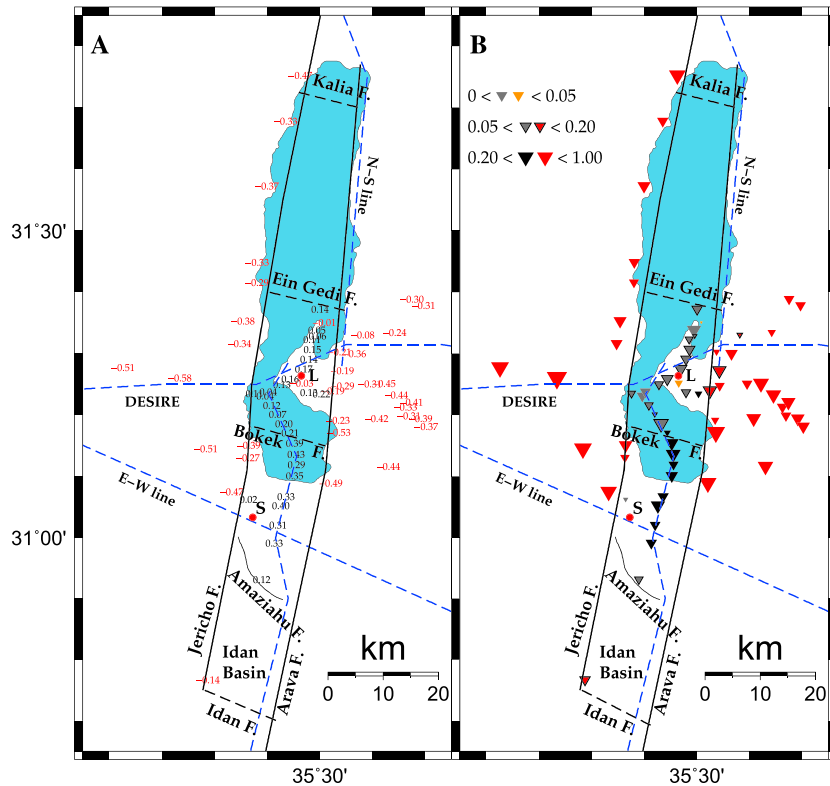


Figure 5. (a) Mean relative teleseismic travel time residuals (seconds; center of the number is the location of the seismic station) that were obtained for the DESIRE stations in the whole DSB. Negative residuals are presented in red. Blue dashed lines present the E-W, N-S, and DESIRE wide-angle reflection/refraction (WRR) profiles of *Ten Brink et al.* [2006], *Ten Brink and Flores* [2012], and *Mechie et al.* [2009], respectively. Main tectonic features are schematically shown (see also Figure 1). Red solid circles present the Lisan 1 (L) and Sodom Deep 1 (S) boreholes; (b) teleseismic travel time residuals of Figure 5a are presented by inverted triangles (red and black colors are for negative and positive anomalies, respectively) whose sizes are proportional to the residuals. In addition, the sizes of small and medium triangles were multiplied by 8 and 2, respectively. Range of values is shown in the upper left corner.

4. Results

Below, we present an overall view of the results, and in the next section we discuss their tectonic implications. For a better understanding of the structure of the basin we use the mean relative teleseismic travel time residuals. The mean relative travel time residuals for all stations using all events are shown in Figure 5. Due to the wide range of azimuths and incidence angles, the mean teleseismic travel time residuals reflect an overall characterization of the relative velocity variations under the DESIRE network. The general pattern is similar to that presented by *Hofstetter et al.* [1991, 2000]. However, in this study, the number of recording stations for each event is significantly larger providing a better station distribution inside the DSB and in its bordering regions.

The mean relative teleseismic travel time residuals are actually a summation of all the anomalies seen by the upcoming rays from the bottom of the model to the top and can be interpreted as a result of crustal changes. To test the influence of the DSB on the upcoming rays for stations that are located on the eastern and western flanks of the basin, we use the mean teleseismic travel time residuals of earthquakes that were originated from the east and the west, for stations that are located on the eastern and western sides, respectively (Figures 6a and 6b). The differences between the teleseismic travel time residuals in Figures 5a and 6a are shown in Figures 6c and 6d. Most of the stations, 18 out of 24, present differences that are less than 0.1 s, showing that the influence of the DSB on the upcoming rays is negligible.

Figure 5 shows mean relative teleseismic travel time residuals in the southern DSB along with main tectonic features. In general, stations situated inside and outside the DSB report positive and negative teleseismic travel time residuals, respectively, essentially delineating the borders of the basin. The Lisan Peninsula is a

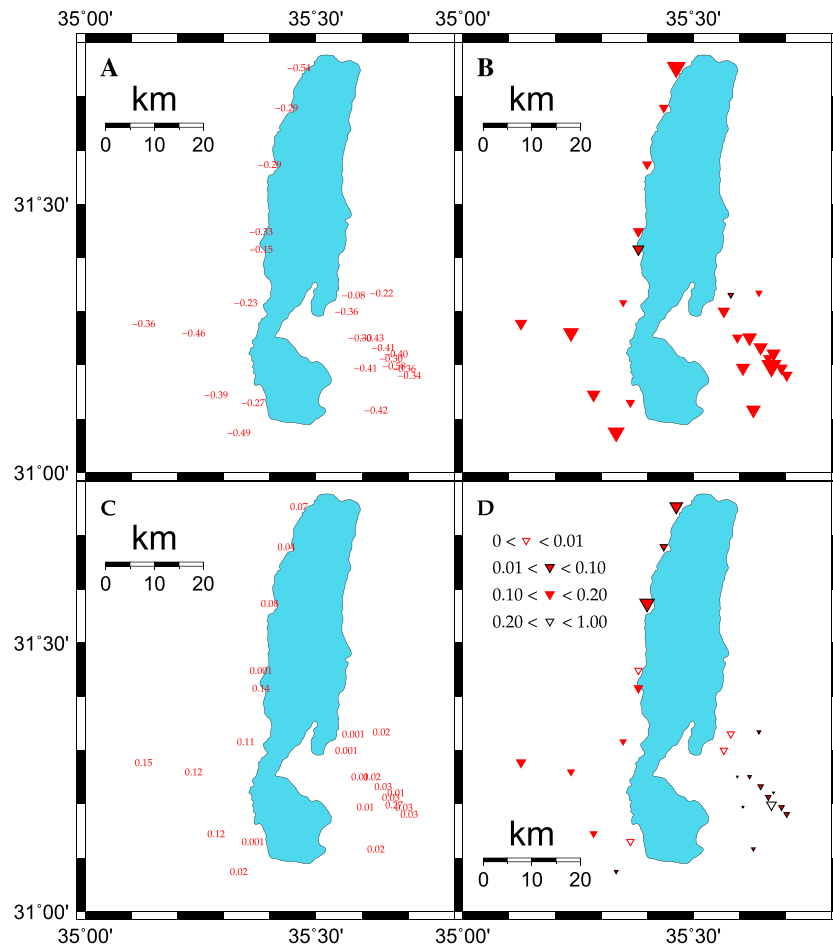


Figure 6. (a) Mean relative teleseismic travel time residuals (seconds; center of the residual value is the location of station) that were obtained for the DESIRE stations based on earthquakes from either east or west for the eastern and western stations, respectively, avoiding the influence of the DSB; (b) residuals of Figure 6a are presented by inverted triangles, with the same color and size designations as Figure 5b; (c) difference between the teleseismic travel time residuals in Figures 5a and 6a for a given station; (d) residuals of Figure 6c are plotted by inverted triangles. The sizes of small, medium, and large triangles were multiplied by 200, 5, and 2, respectively. Range of values is shown in the upper left corner.

large and wide salt dome and several seismic stations were installed on top of it. It is characterized by relatively small positive teleseismic travel time residuals of about 0.14 s, in the latitude range of 31.22 °N–31.37°N and longitude of 35.50 °E, slowly decreasing in a westward direction. Mount Sodom is a significantly smaller salt dome and only one station was installed near the top, obtaining a teleseismic travelttime residual of 0.02 s (just north of the Sodom Deep 1 borehole, Figure 5), and another was installed west of it just off the basin on hard dolomite rock. The largest travelttime residuals are in the southern DSB, south of the Lisan Peninsula in the latitude range of 31.05°N–31.15°N and along longitude 35.45°E and continuing southward toward Amaziahu Fault, reaching values of 0.3 to 0.4 s (Figure 5). We get small positive residual in the Amaziahu Fault and small negative residual about 20 km south of it. East of the southern DSB and the Lisan Peninsula, the mean teleseismic travelttime residuals are negative, having values in the range between –0.21 and –0.53 s with an overall average of –0.35 s. West of the DSB, at distances of up to 20 km and along the margins of the northern and southern Dead Sea basins, the mean teleseismic travelttime residuals are slightly more negative, having values in the range between –0.27 and –0.58 s, with an overall average of –0.45 s.

5. Discussion

The large number of mean relative teleseismic travelttime residuals inside the DSB and in the bordering sides enables a detailed study of the region (Figure 5). The discussion section is divided into two subsections

dealing with first, the spatial distribution of the mean relative teleseismic traveltime residuals, and second, the dimensions of the Lisan and Sodom salt diapirs.

5.1. Spatial Distribution of the Mean Relative Teleseismic Traveltime Residuals

In general, the DSB is characterized by positive values while the bordering regions are negative. We focus our attention on three profiles, the DESIRE WRR crossed the basin in the Lisan Peninsula [Mechie *et al.*, 2009], the E-W line that is located south of the Dead Sea lake [Ten Brink *et al.*, 2006] and N-S line that traverses the Dead Sea basin [Ten Brink and Flores, 2012], allowing us to obtain deeper understanding of the structure of this region (Figures 1 and 5). Along the DESIRE WRR profile [Mechie *et al.*, 2009], the differences between the Lisan Peninsula and the eastern and western sides of the DSB are about 0.5 and 0.6 s, respectively. Based on the latter study, in the shallowest 11 km of the DSB the average velocity is about 4.4 km/s and in the deeper 9 km it is about 6.2 km/s, while on the eastern and western sides for the same depths the values are 5.4 km/s and 6.4 km/s and 5.6 km/s and 6.4 km/s, respectively (Figure 4). Using these velocity differences, especially in the upper part of the crust along the DESIRE WRR profile, the large differences in the mean relative teleseismic traveltime residuals can be easily explained.

In a similar way, we can examine the E-W WRR profile [Ten Brink *et al.*, 2006] (see Figure 5). Along this profile, there are no DESIRE stations on the eastern side and on the western side there are two nearby stations, yielding a difference in the teleseismic traveltime residuals of about 0.8 s. The velocity differences in the first 10 km is about 1.0 km/s and about 0.5 km/s in the depth range from 10 to 18 km. Based on the above mentioned values along the E-W WRR profile, the large differences in the teleseismic traveltime residuals are obvious. Mohsen *et al.* [2011], using receiver function analysis, obtained similar results in which there is an increase in the sediment delay times in the DSB and a decrease to the east.

The N-S WRR line [Ten Brink *et al.*, 2012] (see Figure 5) is composed of two segments. The northern segment is along the eastern shoreline of the Dead Sea lake southward to (35.55°E; 31.25°N). There are only three DESIRE stations that are located near the end of this segment, presenting negative residuals. The southern segment of the N-S line stretches along the western shoreline of the Lisan from (35.45°E; 31.25°N) and then it continues southward in the center of the southern Dead Sea basin along the dams that surround the evaporation ponds. There are 14 DESIRE stations located along the northern part of this segment between latitudes 31.25°N and 31.00°N, presenting relatively small positive residuals near the Lisan Peninsula and larger positive residuals south of latitude 31.15°N, yielding a difference in the teleseismic traveltime residuals of about 0.5 s. Following Ten Brink and Flores [2012], the typical columns in the southern Dead Sea basin and the Lisan Peninsula (southern segment of N-S line) are presented in Figure 4. The velocity difference in the first 4.5 km is about 0.8 km/s. Based on the values along the N-S WRR profile mentioned above, the difference in the teleseismic traveltime residuals of 0.5 s is obvious. Using receiver function analysis Mohsen *et al.* [2011] reported an increase in the sediment delay times in the western part of the southern DSB. In conclusion, the mean teleseismic traveltimes residuals are consistent with the reports of the E-W, N-S and DESIRE WRR profiles [Ten Brink *et al.*, 2006; Mechie *et al.*, 2009], and the receiver function analysis [Mohsen *et al.*, 2011].

The relative teleseismic traveltime residuals clearly delineate the faults on the eastern and western sides of the DSB [Deves *et al.*, 2011; Kagan *et al.*, 2011] (see also Figure 5). Inside the DSB the positive teleseismic residuals are associated with the thick layer of soft material relative to the ambient hard material on both sides of the basin which are associated with negative teleseismic residuals [Ten Brink *et al.*, 2006; Mechie *et al.*, 2009; Ten Brink and Flores, 2012]. The Jordanian highlands on the eastern side of the DSB are of higher altitude than the western side [Segev *et al.*, 2006; Deves *et al.*, 2011]. The bounding flanks of the DSB are geologically different due to the relative left-lateral movement of about 105 km between both sides of the Dead Sea rift. In the Jordanian highlands, on the east side, a sequence of sandstone overlies the granitic rocks while on the western side a limestone-dolomite sequence is exposed [e.g., Ten Brink *et al.*, 1993; Rybakov *et al.*, 1999; Sagy *et al.*, 2003; Bartov *et al.*, 2004; Ten Brink and Flores, 2012]. These geological differences are apparent also in the determined velocity values. Ten Brink *et al.* [2006], Mechie *et al.* [2009], Hofstetter *et al.* [2012], and Braeuer *et al.* [2012b] showed that the eastern side has equal or higher-velocity values than the western side at all depths, from shallow depth down to about 20 km (see Figure 4). Below about 20 km the top of the lower crust on the western side is elevated in comparison to the eastern side, which is composed of faster material [Ten Brink *et al.*, 2006; Mechie *et al.*, 2009; Ten Brink and Flores, 2012]. Thus, if we

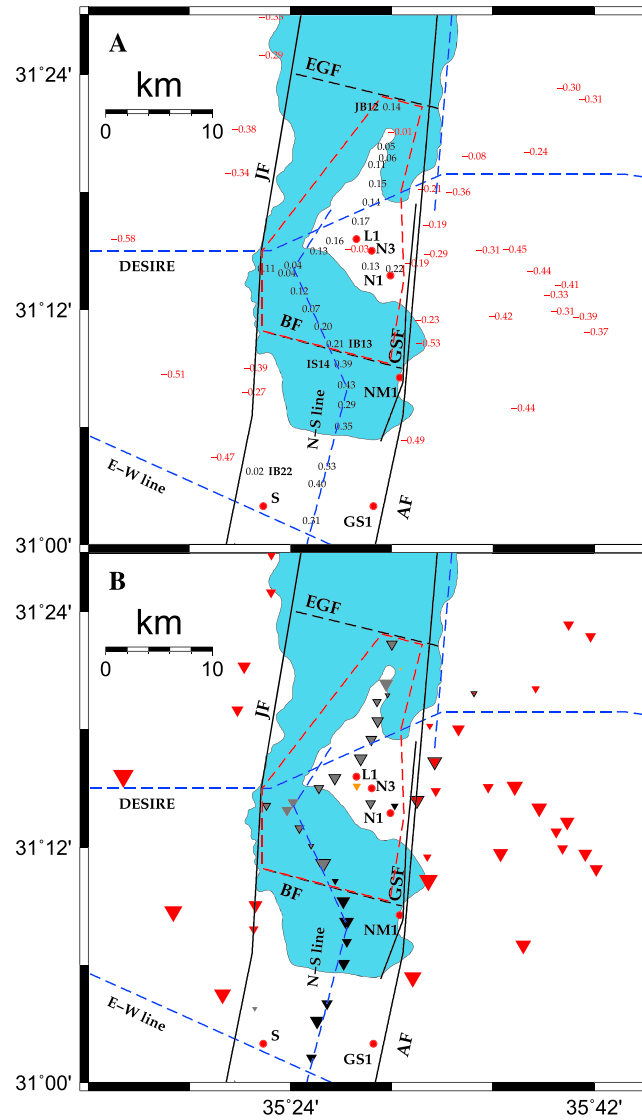


Figure 7. (a) Mean relative teleseismic traveltime residuals (seconds) in the Lisan Peninsula, southern DSB, and surrounding regions. L1, N1, N3, NM1, GS1, and S present the Lisan 1, NRA 1, NRA 3, Numeira 1, and Ghor Safi 1 and Sodom Deep 1 boreholes, respectively. AF, BF, EGF, GSF, JF present the Arava fault, Bokek fault, Ein Gedi fault, Ghor Safi fault, and Jericho fault, respectively. The red dashed line presents the probable limits of the Lisan salt diapir. Stations IB13 and IS14 are located on both sides of the BF, station JB12 is located south of EGF, and station IB22 is on Mount Sodom (near Sodom Deep 1 borehole). See text for further details; (b) residuals of Figure 7a are presented by inverted triangles, where colors and sizes are as in Figure 5b.

Brink, 1989; *Ginzburg and Ben-Avraham*, 1997; *Larsen et al.*, 2002; *Ginzburg et al.*, 2006; *Ben-Avraham and Schubert*, 2006; *Ben-Avraham et al.*, 2008, 2010, and references therein) (Figure 5). The Ein Gedi and Bokek faults border the Lisan Peninsula on the north and south sides, respectively. Based on results of local earthquake tomography, *Braeuer et al.* [2012a, 2012b] reported on strong contrasts in the model of V_P/V_S ratio. Between depths of 2 and 5 km there are observable large ratios (up to 2) north of latitude 31.35°N and south of latitude 31.20°N, which define the Ein Gedi and Bokek faults. Using the teleseismic traveltime residuals, we see a clear change from 0.21 s to 0.39 s at stations IB13 and IS14, respectively, which occurs south of latitude 31.171°N and north of latitude 31.154°N (Figure 7 and Table 1). This change of residual values defines the location of the Bokek fault, which is wholly in agreement with the report of *Braeuer et al.* [2012b].

compare the velocities in the mass columns on both sides of the basin, we obtain near canceling-out effects, but the western mass column is slightly faster overall, rendering to slightly more negative teleseismic traveltime residuals on the western side relative to those on the eastern side.

The Lisan Peninsula, which borders the northern and southern subbasins, and the center of the southern subbasin, are characterized by average positive teleseismic travel time residuals of 0.10 s and 0.36 s, respectively. These observations are fully consistent with the observations of *Ten Brink and Flores* [2012], in which the basin under the Lisan Peninsula is 8–8.5 km deep and shallowing to 5 km deep under Amaziahu fault, about 30 km south of the Lisan Peninsula. The differences in the teleseismic traveltime residuals are due to the existence of a large salt body in the Lisan Peninsula, a relatively fast material, while in the center of the southern subbasin the size of the salt body is significantly smaller. North of the Amaziahu fault (~10 km) the teleseismic traveltime residuals are about 0.3 s gradually decreasing southward in the area of the fault itself to 0.12 s and even becoming negative about 15 km south of the fault. These observations accord well with observations of shallowing and termination of the basin of *Al-Zoubi and ten Brink* [2002], *Ben-Avraham et al.* [2008], *Hofstetter et al.* [2012], and *Ten Brink and Flores* [2012].

The Ein Gedi, Bokek, Amaziahu, and Idan faults, between latitudes 30.7°N and 31.4°N, are four main transverse faults that border the Lisan Peninsula or the southern DSB [*Ben-Avraham and ten*

There are no stations located in the lake itself north of the Lisan Peninsula or north of the Ein Gedi fault (Figure 5). The northernmost station on the Lisan Peninsula is JB12 at latitude 31.372°N (Figure 7 and Table 1), having a small positive residual anomaly of 0.14 s, similar to other neighboring stations in the Lisan Peninsula, located south of this station and near the center of the Lisan Peninsula. This implies that the station is located over the Lisan salt diapir. Since most of the teleseisms occurred at distances of 80° or larger from the station (Figure 2), then the maximal incidence angle relative to the vertical is 20°, or even as low as 15°. We assume a large V_p/V_s ratio change at depth of 5 km, as reported by *Braeuer et al.* [2012b]. In this case, only upcoming rays within horizontal distance of 1.5 km or smaller, originating from earthquakes that are located north of the station, are observed at station JB12. Thus, the Ein Gedi fault is probably located about 2 km north of the station or at approximate latitude of 31.4°N. This result is fully consistent with the report of *Braeuer et al.* [2012b] of large V_p/V_s ratio north of 31.35°N.

The southern DSB is located just south of the Lisan Peninsula, being bordered on the north side by the Bokek fault, in the south by Idan fault, and is bisected by the Amaziahu fault. There is a significant change in the mean relative teleseismic traveltime residuals from an average value of 0.35 s inside the basin to about 0.10–0.15 s in the Lisan Peninsula across the Bokek fault, and across the Amaziahu fault to a value of 0.12 s and even negative south of the fault near the Idan fault (Figure 5). The latter is considered to be the southernmost end of the DSB [*Ben-Avraham et al.*, 2008, and references therein]. The sedimentary sequence thins southward [*Neev and Hall*, 1979; *Ginzburg et al.*, 2006; *Ten Brink and Flores*, 2012]. The single slightly negative teleseismic traveltime residual value near the southwest corner of the Idan basin (Figure 5) supports this observation.

5.2. The Dimensions of the Lisan and Sodom Salt Diapirs

The large number of mean relative teleseismic traveltime residuals inside the DSB and in the bordering sides (Figure 5) enables a better determination of the physical dimensions of the Lisan and the Sodom salt diapirs. In this subsection we focus our attention on the Lisan and Sodom salt diapirs, which are bounded in a relatively small triangle between the E-W line in the southwest, N-S line in the east, and DESIRE WRR in the north (latitudes 31.0–31.4 and longitudes 35.35–35.55). Thus, we assume that the paths away from the Dead Sea basin and near the remote sources, and the paths in the deeper parts of the mantle are highly similar. The changes in the teleseismic traveltime residuals are due to the different structures of the upper crustal columns (Figure 3). The columns in the southern Dead Sea basin and the Lisan Peninsula are similar except that the upper part of the upper crust facilitates the determination of the physical dimensions of the Lisan and the Sodom salt diapirs.

The mean relative teleseismic traveltime residuals in the Lisan Peninsula, with an average value of 0.14 s, are smaller than those in the center of the southern DSB presenting an average value of 0.35 s. The Sodom Deep 1 and Lisan 1 boreholes (S and L in Figure 5) show thick layers of salt of at least 1 km and well over 4 km, respectively [*Abu-Saad and Andrews*, 1993; *Garfunkel and Ben-Avraham*, 1996, 2001; *Gardosh et al.*, 1997; *Al-Zoubi and ten Brink*, 2001]. Salt, despite its relatively low mass density, has unusually high seismic velocity comparable to regular light mass density sedimentary rock but still lower when compared to dolomite or hard limestone [*Dobrin*, 1952]. Thus, one would expect small positive teleseismic traveltimes residuals in the case of stations that are situated above the Lisan salt dome (Figure 5). The density log of Sodom Deep 1 borehole shows a gradual increase of mass density from 2100 kg/m³ close to the surface to about 2400 to 2500 kg/m³ at depths of 4 to 5 km due to compaction, and then it almost levels off at depth of 6.5 km (bottom of the borehole). Throughout the entire borehole the mass density is definitely lower than a comparable dolomite and limestone column.

Several studies using geological and geophysical observations determined the horizontal extension of the Lisan salt diapir. *Al-Zoubi and ten Brink* [2001, and references therein] presented a thorough study of the Lisan salt diapir based on a compilation of magnetic, gravity, and borehole data. They also used a series of reflection lines along the northwest shore of the Lisan Peninsula, crossing the Lisan Peninsula, crossing the southern DSB, and on both sides of the basin. The cross sections in the Lisan Peninsula, i.e., along the northwest shore, present a thick salt layer. The three boreholes, Lisan 1, NRA 1, and NRA 3, in the Lisan Peninsula penetrated a thin cover layer of Lisan marl and then a thick layer of salt, never reaching the bottom of the salt layer. At the Ghor Safi 1 and Numeira 1 boreholes, located south of the Lisan Peninsula, no salt is observed. *Braeuer et al.* [2012b] reported that the V_p model of the Lisan Peninsula

Table 2. Comparison of the Dimensions of the Lisan Salt Diapir as Obtained by Several Studies^a

Geophysical Method	Maximal Horizontal Dimensions (km)	Average (Maximal) Thickness (km)	Authors
Borehole, reflection, gravimetric and magnetic	13 × 10	7.1	<i>Al-Zoubi and ten Brink</i> [2001]
Gravimetric	20 × 10	8 (5.5)	<i>Choi et al.</i> [2011]
Magnetotelluric	17 × 12	5-6	<i>Meqbel et al.</i> [2013]
Seismology	23 × 13	7.2 (4.3)	This study

^aThe values of thickness are the maximal value and average value in parenthesis.

shows no special features. *Choi et al.* [2011] applied 3-D density modeling to new compilations of airborne, shipborne, and terrestrial data sets of Bouguer gravity of the entire DSB. They identified three main salt diapirs: one in the northern Dead Sea subbasin, the Lisan diapir and Mount Sodom diapir. *Meqbel et al.* [2013] conducted a magnetotelluric study across the DSB to obtain the electrical properties of geological and hydrological units. They reported that the Lisan salt body is characterized by very high resistivity, indicating the absence of fluids necessary for electric conductivity. The calculated horizontal dimensions of the Lisan salt diapir following the above-mentioned studies are presented in Table 1. We note that the last two studies suggest a significantly larger salt diapir relative to the calculated dimensions of *Al-Zoubi and ten Brink* [2001].

Observations of teleseismic events can be a useful tool for determining the horizontal dimensions of the Lisan salt diapir, due to the almost vertical arrivals of the incident waves. Thus, high positive values of teleseismic traveltimes residuals of 0.3 s or more, which are observed over most of the southern DSB south of Bokek fault, are due to mainly soft material with relatively small quantities of salt. Small positive residual values that are less than 0.20 s and even as low as -0.03 s represent medium to thick salt layers, respectively. Figure 7 presents average teleseismic traveltimes residuals in the Lisan Peninsula and surrounding regions along with the locations of several boreholes. The Lisan Peninsula is characterized by relatively small positive residuals with an average of about 0.13 s, and some undulations occasionally showing negative values of -0.01 s and -0.03 s. Southwest of the Lisan Peninsula we get slightly smaller values of from 0.04 to 0.12 s. The borehole NRA 1 is located on the southeast side of a large salt body where the thickness of the salt layer is 5.5 km. The salt body is bordered on the east side by the north-south Ghor Safi fault, which is located about 2.0 km west of the Arava fault [*Al-Zoubi and ten Brink*, 2001, Figures 11 and 12]. The teleseismic residual value as obtained from a nearby station is 0.22 s. Thus, we assume that such residual reflects a station near the edge of the salt diapir, as probably some parts of the paths of the upcoming rays may propagate through nonsalt material. Therefore, teleseismic travel time residuals greater than 0.25 s, largely in the southern DSB, indicate relatively soft sediments with little or no salt, and negative teleseismic residuals that are less than -0.10 s, typically on both sides of the basin, are associated with hard rock (i.e., dolomite or hard limestone) likewise without salt. The red dashed line in Figure 7 represents the probable size of the Lisan salt diapir, based on the obtained teleseismic traveltimes residuals. The salt diapir is bounded on the north, west, south, and east sides by the Ein Gedi, Jericho, Bokek, and Ghor Safi faults, respectively. The horizontal dimensions of the salt diapir are about 23 km at its longest place by about 13 km at its widest place. Our estimate is larger than the estimate of *Al-Zoubi and ten Brink* [2001], but with better agreement with the results of *Choi et al.* [2011] and *Meqbel et al.* [2013] (see Table 2).

In the next phase we estimate the thickness of the Lisan salt diapir, based on the differences between the teleseismic traveltimes residuals in the southern DSB and in the Lisan Peninsula. We can use the sedimentary column in the southern DSB as a standard column and compare it with an equivalent column in the Lisan salt diapir, assuming that the salt replaces the soft sediments. *Gardosh et al.* [1997] report that the density log of Sodom Deep 1 borehole shows a gradual increase of mass density from 2100 kg/m^3 close to the surface to about 2400 kg/m^3 to 2500 kg/m^3 at depths of 4 to 5 km, and then it almost levels at depth of 6.5 km (bottom of borehole). Average velocities for the sedimentary column and salt are taken as 3.5 km/s and 4.3 km/s [*Al-Zoubi and ten Brink* [2001]]. Average teleseismic traveltimes residual of the southern DSB is 0.35 s. Figure 8 and Table 2 present calculated thickness of the Lisan salt diapir at each observing station and also a cross section in the sedimentary sequence along the Lisan Peninsula and the dam in the southern Dead Sea basin (right side in Figure 8a). We note the undulations of the thickness of the salt diapir (thick black line in the

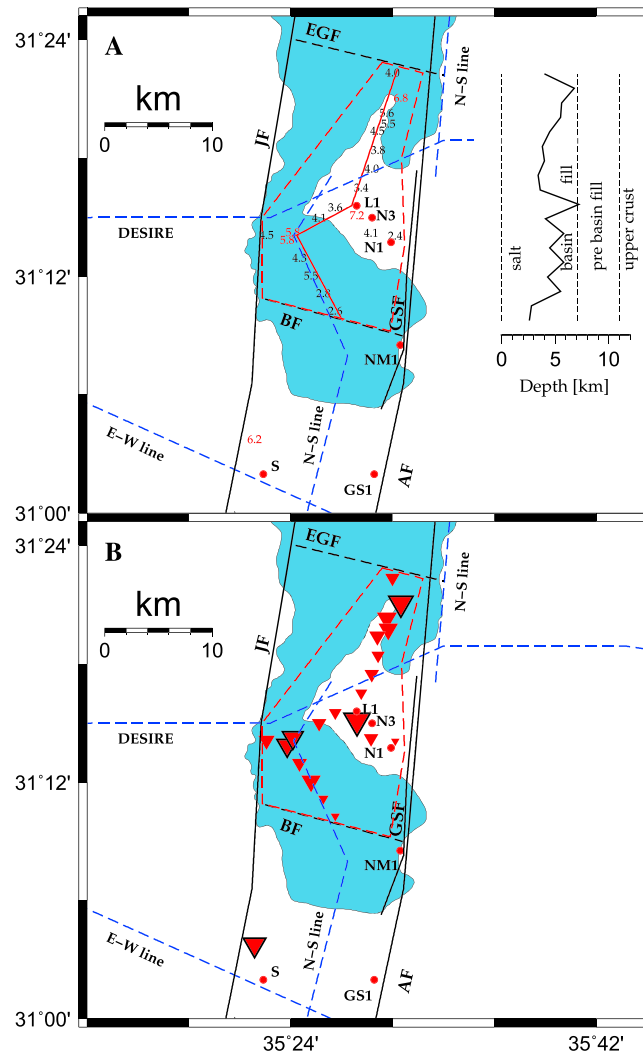


Figure 8. (a) Thickness (kilometers) of salt layer in the Lisan and Sodom diapirs as obtained from the mean relative teleseismic traveltime residuals. Red numbers present local maximal thickness of the salt exceeding 5.5 km. The red solid line presents the location of a cross section of the sedimentary section (right side) through the Lisan Peninsula and along the N-S line in the dam in the southern Dead Sea basin. Dashed black lines in the cross section present the sedimentary sequence of Figure 4, and solid black line present the thickness in km of the salt diapir along the cross section. See Figure 7 for more information; (b) residuals of Figure 8a are presented by inverted triangles, where sizes are proportional to thickness. Inverted triangles with black frame present local maximal thickness of the salt exceeding 5.5 km.

western and eastern sides of Sodom salt diapir, respectively, are composed of light and slow sediments (see stratigraphic sections in Stein [2001], Bartov and Sagy [2004], Ben-Avraham et al. [2008, and references therein]). One can expect positive teleseismic traveltime residuals of 0.3 s or more for stations that are located in the Amiaz plain and southern Dead Sea basin. In the DESIRE campaign only one station (IB22, see Table 1) was operating near the center of the diapir with mean relative teleseismic traveltime residual of 0.02 s suggesting a thickness of 6.2 km (Figure 8). The relative small residual value of 0.02 s rules out the possibility that the upcoming rays were propagating in the Amiaz plain or southern Dead Sea basin. Our result is comparable with the suggested thickness of Gardosh et al. [1997] and Ginzburg et al. [2006] and larger than the thickness of 4 km as suggested by Choi et al. [2011].

cross section in Figure 8a), where away from the center the determined thicknesses are normally smaller. The mean teleseismic traveltimes residual at the center of the Lisan salt diapir is -0.03 s (west of borehole NRA 3, Figure 7), thus suggesting that the maximal thickness of the salt layer is 7.2 km. The picking error is estimated to be less than 0.02 s, which suggests a thickness error of about 80 m. This value is comparable with the maximum value of 7.1 km of Al-Zoubi and ten Brink [2001] near NRA 3 and 8 km of Choi et al. [2011]. The thickness in the other parts of the Lisan salt diapir is not uniform, varying between 3.6 km and 5.8 km with an average thickness of 4.3 km, except for a high value of 6.8 in the northern part of the diapir just south of the Ein Gedi fault, and low values of 2.6 km and 2.8 km near the Bokek fault. The average thickness is smaller than the estimates of 5.5 km and 5–6 km of Choi et al. [2011] and Meqbel et al. [2013], respectively (see Table 2).

In a similar manner we can estimate the thickness of Mount Sodom salt diapir. Sodom salt diapir is significantly smaller than the Lisan salt diapir. Gardosh et al. [1997] and Ginzburg et al. [2006], using measurements at Sodom Deep 1 borehole and reflection studies, suggested that the diapir may stem from a salt layer that is located at a depth of 5–6 km with thickness of less than 1 km. Based on the observed seismic activity at Mount Sodom, Hofstetter et al. [2012] reported that the entire structure is relatively shallow with no deep roots. The diapir is surrounded by the Amiaz plain and the southern Dead Sea basin on the

6. Conclusions

We study the structure of the Dead Sea basin and its neighboring regions using *P* and *PKP* wave relative travel time residuals of 644 teleseisms, as recorded by the DESIRE portable seismic network. Based on the teleseismic residuals our findings of the structure are as follows:

1. The Lisan Peninsula is characterized by relatively small teleseismic traveltime residuals of about 0.14 s, in the latitude range of 31.22°N–31.37°N and at the longitude of 35.50°E, slowly decreasing toward the west. The southern Dead Sea basin, south of the Lisan Peninsula in the latitude range of 31.05°N–31.15°N and along longitude 35.45°E and continuing southward toward the Amaziahu fault, is characterized by the largest positive teleseismic traveltime residuals reaching values of 0.4–0.5 s. The above mentioned anomalies are consistent with thick layers of salt and soft sediments in the upper part of the upper crust (Figure 3), respectively, as was shown in reports of the E-W, N-S and DESIRE WRR profiles [Ten Brink *et al.*, 2006; Mechie *et al.*, 2009], and the receiver function analysis [Mohsen *et al.*, 2011].
2. The mean teleseismic traveltime residuals, east of the southern DSB and the Lisan Peninsula, are negative, having values in the range between –0.21 s and –0.53 s with an overall average of –0.35 s. West of the DSB, at distances of up to 20 km and along the margins of the northern and southern Dead Sea basins, the mean teleseismic traveltime residuals are slightly more negative having values in the range between –0.27 s and –0.58 s, with an overall average of –0.45 s. These observations are consistent with the report of the DESIRE WRR profile [Mechie *et al.*, 2009] and the receiver function analysis [Mohsen *et al.*, 2011].
3. Using the teleseismic residuals we estimate the horizontal dimensions of the Lisan salt diapir to be 23 km × 13 km at its widest and a maximal thickness of about 7.2 km. The thickness of the Mount Sodom salt diapir is estimated as 6.2 km.
4. The changes of teleseismic traveltime residuals, in the stations on the dams of the evaporation ponds, define the location of the Bokek fault south of latitude 31.171°N and north of latitude 31.154°N or about 31.16°N, in full agreement with the report of Braeuer *et al.* [2012b].
5. There are no stations located in the Dead Sea lake itself north of the Lisan Peninsula or north of the Ein Gedi fault (Figure 5), which bounds the Lisan Peninsula on the northern side. However, based on the teleseismic traveltime residual in the northernmost station in the Lisan Peninsula and the report of Braeuer *et al.* [2012b], the Ein Gedi fault is probably located about 2 km north of the station or about latitude 31.38°N.
6. The DESIRE project provided important and detailed information regarding the southern Dead Sea basin. However, an extensive study of both diapirs is still needed involving many seismic stations which can provide a more accurate determination of the physical dimensions of the salt diapirs.

Acknowledgments

The study was supported by EOST, University of Strasbourg, France, Chaire Gutenberg Strasbourg, France, ORSTOM, France, and the Earth Sciences and Research Administration, Ministry of Energy and Water, Israel. A. Hofstetter thanks the Région Alsace and the Communauté Urbaine de Strasbourg for the award of a Gutenberg Excellence Chair. Some figures in this report were prepared using the GMT program [Wessel and Smith, 1991]. Constructive comments of A. Agnon and two anonymous reviewers significantly improved the manuscript. We thank T. Goepfert and L. Lepine for helping us in data processing. We thank the Geophysical Instrument Pool Potsdam for providing the instruments for the DESIRE experiments and GEOFON for data archiving.

References

- Abu-Saad, L., and I. Andrews (1993), A database of stratigraphic information from deep boreholes in Jordan, *Natural Resources Authority, Jordan, Subsurf. Geol.*, *6*, 1–182.
- Aldersons, F., Z. Ben-Avraham, A. Hofstetter, E. Kissling, and T. Al-Yazjeen (2003), Lower-crustal strength under the Dead Sea basin from local earthquake and rheological modeling, *Earth Planet. Sci. Lett.*, *214*, 129–142.
- Al-Zoubi, A., and U. S. ten Brink (2001), Salt diapirs in the Dead Sea basin and their relationship to Quaternary extensional tectonics, *Mar. Pet. Geol.*, *18*, 779–797.
- Al-Zoubi, A., and U. S. ten Brink (2002), Lower crustal flow and the role of shear in basin subsidence: An example from the Dead Sea basin, *Earth Planet. Sci. Lett.*, *199*, 67–79, doi:10.1016/S0012-821X(02)00540-X.
- Al-Zoubi, A., H. Shulman, and Z. Ben-Avraham (2002), Seismic reflection profiles across the southern Dead Sea basin, *Tectonophysics*, *346*, 61–69.
- Al-Zoubi, A., T. Heinrichs, M. Sauter, and U. S. ten Brink (2007), The northern end of the Dead Sea basin: Geometry from reflection seismic evidence, *Tectonophysics*, *434*, 55–69.
- Bartov, Y., and A. Sagy (2004), Late Pleistocene extension and strike-slip in the Dead Sea basin, *Geol. Mag.*, *141*, 565–572, doi:10.1017/S001675680400963X.
- Bartov, Y., A. Agnon, Y. Enzel, and M. Stein (2006), Late Quaternary faulting and subsidence in the central Dead Sea basin, *Isr. J. Earth Sci.*, *55*, 17–31.
- Ben-Avraham, Z. (1997), Geophysical framework of the Dead Sea: Structure and tectonic, in *The Dead Sea, the Lake and its Settings*, *Oxford Monogr. Geol. Geophys.*, vol. 36, edited by T. M. Niemi, Z. Ben-Avraham, and J. R. Gat, pp. 22–35, Oxford Univ. Press, New York.
- Ben-Avraham, Z., and A. Ginzburg (1990), Displaced terranes and crustal evolution of the Levant and the eastern Mediterranean, *Tectonics*, *9*, 613–622, doi:10.1029/TC009i004p00613.
- Ben-Avraham, Z., and G. Schubert (2006), Deep “drop down” basin in the southern Dead Sea, *Earth Planet. Sci. Lett.*, *251*, 254–263.
- Ben-Avraham, Z., and U. ten Brink (1989), Transverse faults and segmentation of basins within the Dead Sea rift, *J. Afr. Earth Sci.*, *8*, 603–616.
- Ben-Avraham, Z., Z. Garfunkel, and M. Lazar (2008), Geology and evolution of the southern Dead Sea fault with emphasis on subsurface structure, *Annu. Rev. Earth Planet. Sci.*, *36*, 357–387.
- Ben-Avraham, Z., V. Lyakhovskiy, and G. Schubert (2010), Drop-down formation of deep basins along the Dead Sea and other strike-slip fault systems, *Geophys. J. Int.*, *181*, 185–197, doi:10.1111/j.1365-246X.2010.04525.x.

- Ben-Menahem, A., A. Nur, and M. Vered (1976), Tectonics, seismicity and structure of the Afro-Eurasian junction—the breaking of an incoherent plate, *Phys. Earth Planet. Inter.*, *12*, 1–50.
- Braeuer, B., G. Asch, A. Hofstetter, C. Haberland, D. Jaser, R. El-Kelani, and M. Weber (2012a), Microseismicity distribution in the southern Dead Sea area and its implications on the structure of the basin, *Geophys. J. Int.*, *188*, 873–878.
- Braeuer, B., G. Asch, A. Hofstetter, C. Haberland, D. Jaser, R. El-Kelani, and M. Weber (2012b), High resolution local earthquake tomography of the southern Dead Sea area, *Geophys. J. Int.*, *191*, 881–897, doi:10.1111/j.1365-246X.2012.05668.x.
- Braeuer, B., G. Asch, A. Hofstetter, C. Haberland, D. Jaser, R. El-Kelani, and M. Weber (2014), Detailed seismicity analysis revealing the dynamics of the southern Dead Sea area, *J. Seismolog.*, *18*, doi:10.1007/s10950-014-9441-4.
- Choi, S., H.-J. Götte, U. Meyer, and DESIRE Group (2011), 3-D density modelling of underground structures and spatial distribution of salt diapirism in the Dead Sea basin, *Geophys. J. Int.*, *184*, 1131–1146, doi:10.1111/j.1365-246X.2011.04939.x.
- Deves, M., G. C. P. King, Y. Klinger, and A. Agnon (2011), Localised and distributed deformation in the lithosphere: Modelling the Dead Sea region in 3 dimensions, *Earth Planet. Sci. Lett.*, *308*, 172–184, doi:10.1016/j.epsl.2011.05.044.
- Dobrin, M. B. (1952), *Introduction to Geophysical Prospecting*, McGraw-Hill, New York.
- Dorbath, C., L. Dorbath, J. D. Fairhead, and G. W. Stuart (1986), A teleseismic delay time study across the Central African shear zone in the Adamawa region of Cameroon, *Geophys. J. R. Astron. Soc.*, *86*, 751–766.
- Dorbath, C., D. Oppenheimer, F. Amelung, and G. King (1996), Seismic tomography and deformation modeling of the junction of the San Andreas and Calaveras faults, *J. Geophys. Res.*, *101*, 27,917–27,941, doi:10.1029/96JB02092.
- El-Isa, Z. (1990), Lithospheric structure of the Jordan-Dead Sea transform from earthquake data, *Tectonophysics*, *180*, 29–36.
- El-Isa, Z., J. Mechie, C. Prodehl, J. Makris, and R. Rihm (1987), A crustal structure study of Jordan derived from seismic refraction data, *Tectonophysics*, *138*, 235–253.
- Ellsworth, W. L., and R. Koyanagi (1977), Three-dimensional crust and mantle structure of Kilauea Volcano, Hawaii, *J. Geophys. Res.*, *82*, 5379–5394, doi:10.1029/JB082i033p05379.
- Engdahl, R., J. Sindorf, and R. Epply (1977), Interpretation of relative teleseismic P wave residuals, *J. Geophys. Res.*, *82*, 5671–5682, doi:10.1029/JB082i036p05671.
- Freund, R., Z. Garfunkel, I. Zak, M. Goldberg, T. Weissbrod, and B. Derin (1970), The shear along the Dead Sea rift, *Philos. Trans. R. Soc. A*, *267*, 107–130.
- Frieslander, U. (2000), The structure of the Dead Sea transform emphasizing the Arava, using new geophysical data, PhD thesis, 101 pp., Hebrew Univ. of Jerusalem, Jerusalem, Israel.
- Gardosh, M., E. Kashai, S. Sallhov, H. Shulman, and E. Tannenbaum (1997), Hydrocarbon exploration in the southern Dead Sea basin, in *The Dead Sea, the Lake and its Settings*, *Oxford Monogr. Geol. Geophys.*, vol. 36, edited by T. M. Niemi, Z. Ben-Avraham, and J. R. Gat, pp. 57–72, Oxford Univ. Press, New York.
- Garfunkel, Z. (1981), Internal structure of the Dead Sea leaky transform (rift) in relation to plate kinematics, *Tectonophysics*, *80*, 81–108.
- Garfunkel, Z., and Z. Ben-Avraham (1996), The structure of the Dead Sea basin, *Tectonophysics*, *266*, 155–176.
- Garfunkel, Z., and Z. Ben-Avraham (2001), Basins along the Dead Sea transform, in *PeriTethyan Rift/Wrench Basins in Passive Margins*, *Memo. Mus. Natl. Hist. Nat.*, vol. 186, edited by P. A. Ziegler et al., pp. 607–627, Elsevier, Amsterdam.
- Garfunkel, Z., I. Zak, and R. Freund (1981), Active faulting in the Dead Sea rift, *Tectonophysics*, *80*, 1–26.
- Ginzburg, A., and Z. Ben-Avraham (1997), A seismic refraction study of the north basin of the Dead Sea, Israel, *Geophys. Res. Lett.*, *24*, 2063–2066, doi:10.1029/97GL01884.
- Ginzburg, A., and Y. Folkman (1980), The crustal structure between the Dead Sea rift and the Mediterranean Sea, *Earth Planet. Sci. Lett.*, *51*, 181–188.
- Ginzburg, A., J. Makris, K. Fuchs, C. Prodehl, W. Kaminski, and U. Amitai (1979a), A seismic study of the crust and upper mantle of the Jordan-Dead Sea rift and their transition toward the Mediterranean sea, *J. Geophys. Res.*, *84*, 1569–1582, doi:10.1029/JB084iB04p01569.
- Ginzburg, A., J. Makris, K. Fuchs, B. Perathoner, and C. Prodehl (1979b), Detailed structure of the crust and upper mantle along the Jordan-Dead Sea rift, *J. Geophys. Res.*, *84*, 5605–5612, doi:10.1029/JB084iB10p05605.
- Ginzburg, A., J. Makris, K. Fuchs, and C. Prodehl (1979c), The structure of the crust and upper mantle in the Dead Sea rift, *Tectonophysics*, *80*, 109–119.
- Ginzburg, A., M. Reshef, Z. Ben-Avraham, and U. Schattner (2006), The style of transverse faulting in the Dead Sea basin from seismic reflection data: The Amazyahu fault, *Isr. J. Earth Sci.*, *55*, 129–139.
- Hofstetter, A., L. Feldman, and Y. Rotstein (1991), Crustal structure of Israel: Constraints from teleseismic and gravity data, *Geophys. J. Int.*, *104*, 371–379.
- Hofstetter, A., C. Dorbath, M. Rybakov, and V. Goldshmidt (2000), Crustal and upper mantle structure across the Dead Sea rift and Israel from teleseismic P wave tomography and gravity data, *Tectonophysics*, *327*, 37–59.
- Hofstetter, A., Y. Klinger, A. Amrat, L. Rivera, and L. Dorbath (2007), Stress inversion and focal mechanisms along the Levantine Fault from seismological data, *Tectonophysics*, *429*, 165–181.
- Hofstetter, A., Y. Gitterman, V. Pinsky, N. Kraeva, and L. Feldman (2008), Seismological observations of the Northern Dead Sea basin earthquake on 11/2/2004, *Isr. J. Earth Sci.*, *57*, 101–124.
- Hofstetter, A., C. Dorbath, and M. Calò (2012), Crustal structure of the Dead Sea basin from local earthquake tomography, *Geophys. J. Int.*, *189*, 554–568.
- Kagan, E., M. Stein, A. Agnon, and F. Neumann (2011), Intrabasin paleoearthquake and quiescence correlation of the late Holocene Dead Sea, *J. Geophys. Res.*, *116*, B04311, doi:10.1029/2010JB007452.
- Kashai, E. L., and P. F. Croker (1987), Structural geometry and evolution of the Dead Sea-Jordan rift system as deduced from new subsurface data, *Tectonophysics*, *141*, 33–60.
- Kaviani, A., A. Hofstetter, G. Rumpker, and M. Weber (2013), Investigation of seismic anisotropy beneath the Dead Sea fault using dense networks of broadband stations, *J. Geophys. Res. Solid Earth*, *118*, 3476–3491, doi:10.1002/jgrb.50250.
- Kennett, B., and R. Engdahl (1991), Travel times for global earthquake location and phase association, *Geophys. J. Int.*, *105*, 429–465.
- Koulakov, I., and S. V. Sobolev (2006), Moho depth and three-dimensional P and S structure of the crust and uppermost mantle in the Eastern Mediterranean and Middle East derived from tomographic inversion of local ISC data, *Geophys. J. Int.*, *164*, 218–235, doi:10.1111/j.1365-246X.2005.02791.x.
- Koulakov, I., S. V. Sobolev, M. Weber, S. Oreshin, K. Wylegalla, and A. Hofstetter (2006), Teleseismic tomography reveals no signature of the Dead Sea transform in the upper mantle structure, *Earth Planet. Sci. Lett.*, *252*, 189–200, doi:10.1016/j.epsl.2006.09.039.
- Larsen, B. D., Z. Ben-Avraham, and H. Shulman (2002), Fault and salt tectonics in the southern Dead Sea basin, *Tectonophysics*, *346*, 71–90.
- Lazar, M. (2004), Tectonic processes along the northern edges of pull-apart basins in the Dead Sea rift: A case study from the Northern Dead Sea, PhD thesis, 156 pp., Tel Aviv Univ., Tel Aviv, Israel.

- Lazar, M., Z. Ben-Avraham, and U. Schattner (2006), Formation of sequential basins along a strike-slip fault—Geophysical observations from the Dead Sea basin, *Tectonophysics*, *421*, 53–69.
- Mechie, J., K. Abu-Ayyash, Z. Ben-Avraham, R. El-Kelani, A. Mohsen, G. Rumpker, J. Saul, and M. Weber (2005), Crustal shear velocity structure across the Dead Sea transform from two-dimensional modelling of DESERT project explosion seismic data, *Geophys. J. Int.*, *160*, 910–924, doi:10.1111/j.1365-246X.2005.02526.x.
- Mechie, J., K. Abu-Ayyash, Z. Ben-Avraham, R. El-Kelani, I. Qabbani, M. Weber, and DESIRE Group (2009), Crustal structure of the southern Dead Sea basin derived from project DESIRE wide-angle seismic data, *Geophys. J. Int.*, *178*, 457–478.
- Meqbel, N., O. Ritter, and DESIRE Group (2013), A magnetotelluric transect across the Dead Sea basin: Electrical properties of geological and hydrological units of the upper crust, *Geophys. J. Int.*, *193*, 1415–1431.
- Mohsen, A., G. Asch, J. Mechie, R. Kind, A. Hofstetter, M. Weber, M. Stiller, and K. Abu-Ayyash (2011), Crustal structure of the Dead Sea basin (DSB) from a receiver function analysis, *Geophys. J. Int.*, *184*, 463–476.
- Neev, D., and J. K. Hall (1979), Geophysical investigations in the Dead Sea, *Sediment. Geol.*, *23*, 209–238.
- Ozakin, Y., Y. Ben-Zion, M. Aktar, H. Karabulut, and Z. Peng (2012), Velocity contrast across the 1944 rupture zone of the North Anatolian fault east of Ismetpasa from analysis of teleseismic arrivals, *Geophys. Res. Lett.*, *39*, L08307, doi:10.1029/2012GL051426.
- Petrinin, A. G., and S. V. Sobolev (2006), What controls thickness of sediments and lithospheric deformation at a pull-apart basin?, *Geology*, *34*, 389–392.
- Petrinin, A. G., and S. V. Sobolev (2008), Three-dimensional numerical models of the evolution of pull-apart basins, *Phys. Earth Planet. Inter.*, *171*, 387–399.
- Reasenber, P., W. Ellsworth, and A. Walter (1980), Teleseismic evidence for a low-velocity body under the Coso geothermal area, *J. Geophys. Res.*, *85*, 2471–2483, doi:10.1029/JB085iB05p02471.
- Rotstein, Y., Y. Bartov, and A. Hofstetter (1991), Active compressional tectonics in the Jericho area, Dead Sea rift, *Tectonophysics*, *198*, 239–259.
- Rybakov, M., V. Goldshmidt, Y. Rotstein, L. Fleischer, I. Goldberg, C. Campbell, and P. Millegan (1999), Petrophysical constraints on gravity/magnetic interpretation in Israel, *Leading Edge*, *18*, 269–272, doi:10.1190/1.1438274.
- Sagy, A., Z. Reches, and A. Agnon (2003), Hierarchic three-dimensional structure and slip partitioning in the western Dead Sea pull-apart, *Tectonics*, *22*(1), 1004, doi:10.1029/2001TC001323.
- Segev, A., M. Rybakov, A. Hofstetter, Z. Ben-Avraham, and G. Tibor (2006), The structure, isostasy and gravity field of the Levant continental margin and the southeast Mediterranean area, *Tectonophysics*, *425*, 137–157.
- Shamir, G. (2006), The active structure of the Dead Sea depression, *Spec. Pap. Geol. Soc. Am.*, *401*, 15–32.
- Shamir, G., Y. Eyal, and I. Bruner (2005), Localized versus distributed shear in transform plate boundary zones: The case of the Dead Sea transform in the Jericho Valley, *Geochem. Geophys. Geosyst.*, *6*, Q05004, doi:10.1029/2004GC000751.
- Stein, M. (2001), The sedimentary and geochemical record of Neogene-Quaternary water bodies in the Dead Sea basin—Inferences for the regional paleoclimatic history, *J. Paleolimnol.*, *26*, 271–82.
- Storchak, D., J. Schweitzer, and P. Bormann (2003), The IASPEI standard seismic phase list, *Seismol. Res. Lett.*, *74*, 761–772.
- Ten Brink, U., and C. Flores (2012), Geometry and subsidence history of the Dead Sea basin: A case for fluid-induced mid-crustal shear zone?, *J. Geophys. Res.*, *117*, B01406, doi:10.1029/2011JB008711.
- Ten Brink, U. S., Z. Ben-Avraham, R. E. Bell, M. Hassouneh, D. F. Coleman, G. Andreasen, G. Tibor, and B. Coakley (1993), Structure of the Dead Sea pull-apart basin from gravity analyses, *J. Geophys. Res.*, *98*(B12), 21,877–21,894, doi:10.1029/93JB02025.
- Ten Brink, U. S., A. S. Al-Zoubi, C. H. Flores, Y. Rotstein, I. Qabbani, S. H. Harder, and G. R. Keller (2006), Seismic imaging of deep low-velocity zone beneath the Dead Sea basin and transform fault: Implications for strain localization and crustal rigidity, *Geophys. Res. Lett.*, *33*, L24314, doi:10.1029/2006GL027890.
- Van Eck, T., and A. Hofstetter (1989), Microearthquake activity in Dead Sea region, *Geophys. J. Int.*, *99*, 605–620.
- Van Eck, T., and A. Hofstetter (1990), Fault geometry and spatial clustering of microearthquakes along the Dead Sea-Jordan fault zone, *Tectonophysics*, *180*, 15–27.
- Weber, M. (2005), Crustal shear velocity structure across the Dead Sea transform from two-dimensional modelling of DESERT project explosion seismic data, *Geophys. J. Int.*, *160*, 910–924, doi:10.1111/j.1365-246X.2005.02526.x.
- Weber, M., and DESERT Group (2004), The crustal structure of the Dead Sea transform, *Geophys. J. Int.*, *156*, 655–681, doi:10.1111/j.1365-246X.2004.02143.x.
- Weber, M., and DESIRE group (2009), Anatomy of the Dead Sea transform from lithospheric to microscopic scale, *Rev. Geophys.*, *47*, RG2002, doi:10.1029/2008RG000264.
- Wessel, P., and W. Smith (1991), Free software helps map and display data, *Eos Trans. AGU*, *72*, 441–446, doi:10.1029/90EO00319.